Dalton Transactions

ROYAL SOCIETY OF CHEMISTRY

PAPER

View Article Online
View Journal | View Issue

Cite this: *Dalton Trans.*, 2026, **55**, 3323

Infection microenvironment-responsive composites based on a Ag(I) complex for targeted antimicrobial treatment

Jing Han, *[a] Yue Hou,[a] Zhong Yu,*[b] Yi-xuan Chen,[a] Jian-fei Xue,[a] Yue-juan Zhang,[c] Lei Gao[c] and Yi Wan*[c]

Received 13th November 2025,
Accepted 23rd January 2026

DOI: 10.1039/d5dt02724a

rsc.li/dalton

To address always-on Ag^+ release of Ag(I) complexes for antimicrobial treatment, infection microenvironment-responsive composites with high antimicrobial efficiency and on-demand Ag^+ release were constructed by coating hyaluronic acid (HA) or an Fe(III)–tannic acid complex (Fe(III)–TA) on a deliberately designed silver complex (**1**) with a high silver content of 46.76%. The targeted Ag^+ leaching to eradicate bacteria was dependent on stimuli-responsive coating decomposition. Infection microenvironment cues, *i.e.* hyaluronidase (HAase) and acidity, were used as endogenous triggers, and the wrapped complex **1** acted as a carrier for antimicrobial Ag^+. This smart design can avoid the use of additional carriers for the antimicrobial agents required in previous approaches and reduces the side effects of degradation in the infection microenvironment. Complex **1** was characterized by single-crystal X-ray diffraction as a 1D chain assembled from Ag_{12} clusters. It exhibits effective broad-spectrum antimicrobial activities with low minimum inhibition concentrations (MICs) originating from high Ag^+ content. Under non-infection conditions, Ag^+ release ratios of **1**@HA and **1**@Fe(III)–TA were suppressed significantly to 14.99% and 3.31%, respectively. In a simulated infection microenvironment (1 wt% HAase or pH 5.5), the composites exhibited stimulus-switched coating disassembly, leading to increased Ag^+ release ratios of 59.26% and 23.92%, respectively. The moderate pH-induced Ag^+ release of **1**@Fe(III)–TA was attributed to partial cleavage of Fe–OH of Fe(III)–TA at pH 5.5, which was verified by the pH-dependent Ag^+ release of **1**@Fe(III)–TA. The stimuli-responsive coating deconstruction and the antimicrobial performance of the two composites were confirmed by measurements of water contact angles, zeta potentials, inhibition zones, and MICs. **1**@Fe(III)–TA displayed more obvious acid-triggered performance for *P. aeruginosa* and carbapenem-resistant *E. coli* due to their stronger acid-producing characteristics. The successful integration of an efficient antimicrobial Ag(I) complex with infection microenvironment-responsive coatings highlights its potential as a facile strategy for on-demand antimicrobial treatment of targeted bacterial infection.

Introduction

Microbial infections pose an alarming and pressing global health concern. Unfortunately, the prevalent treatments with antibiotics have notably accelerated microbial resistance. Metal-ion-containing materials that demonstrate efficient antimicrobial activities[1,2] with distinct antimicrobial mechanisms as conventional antibiotics[3,4] have emerged as innovative solutions due to their potential as promising alternatives to antibiotics that can address antimicrobial resistance.[5] Their antimicrobial activities stem from metal cations[6] (*e.g.* Ag^+,[7] Cu^{2+},[8] Zn^{2+},[9] and Fe^{2+} [10]) in the materials, which can oxidize and destroy the integrity of the bacterial membrane,[11] interrupt the respiratory chain,[12] and interfere with DNA replication, to damage the lipids.[13] The physical damage process for bacterial cells displays low drug-resistance risk for microbial elimination with high antimicrobial efficacy. Silver ion materials, including silver nanoparticles,[14] silver polymers,[15] silver complexes,[16] and silver-doped composites,[17–19] have been especially developed because of their superior antimicrobial effects[20] with broad-spectrum action,[21] lower toxicity,[22] and photo-thermal stability.[23] Among these, silver complexes represent a class of hybrid materials that are composed of silver ion nodes connected with organic linkers through coordination bonds. They can serve as silver ion reservoirs that delay the rapid release of Ag^+ and avoid severe cytotoxicity,[24] benefiting from their robust structural features.[25] Self-assembly of Ag^+

[a]*Department of Materials Physics and Chemistry, Xi'an University of Technology, Xi'an, Shaanxi, 710048, China*
[b]*Department of Applied Chemistry, Xi'an University of Technology, Xi'an, Shaanxi, 710048, China. E-mail: yuzhong@xaut.edu.cn*
[c]*Microbiology Institute of Shaanxi, Xi'an, Shaanxi, 710043, China. E-mail: wanyi6565@163.com*

with antimicrobial ligands can further realize synergistic antimicrobial effects of '1 + 1 > 2'.[26] However, the sustained release of Ag^+ from the pristine complex is generally passive and uncontrolled, which can cause unregulated concentrations of Ag^+, leading to biological toxicity and resource waste.[27] Thus, developing silver complexes equipped with controlled and on-demand Ag^+ release triggers solely at the site of microbial infection are urgently needed for mitigating premature leakage of Ag^+.

Stimuli-responsive materials, as smart and innovative platforms, could generate a controlled response upon contact with specific stimuli classified as external (exogenous) and internal (endogenous). External stimuli, such as temperature, light, and magnetic fields, from the outside environment, can be utilized to trigger the release of encapsulated agents at the desired time. Internal stimuli refer to triggers inside the target microenvironment, including high expression of specific enzymes (*e.g.* hyaluronidase, HAase),[28] high secretions of organic acids,[29] and elevated levels of ROS.[30] Various intelligent strategies have been reported with the fundamental principle of achieving controlled delivery in response to external and/or internal stimuli. Presently, stimuli-responsive materials based on complexes are mainly investigated as carriers for cancer drug release and biological imaging, whereas evaluations of stimuli-responsive complexes for antimicrobial therapy are relatively scarce. Functionalization of carriers or modification of antimicrobial agents with stimuli-responsive components or groups represents an effective strategy for targeted antimicrobial treatment. For example, Zhang *et al.* constructed an antimicrobial platform by coating hyaluronic acid (HA) on Ag^+-loaded metal–organic frameworks (MOFs)[31] and achieved controlled HAase-responsive release of Ag^+ through hydrolysis of HA triggered by HAase.[32] Gu *et al.* designed a pH-responsive doxorubicin (DOX) encapsulated polymeric micelle assembled with a pH-sensitive citraconic amide,[33] which demonstrated targeted release of DOX at pH 5.5.[34] Other stimuli-responsive release materials were developed, as reviewed elsewhere, to fight against bacterial infection.[35–38]

We have concentrated on structures of Ag(I) complexes[39,40] and their antimicrobial effects.[41,42] Our results confirmed that their antimicrobial efficiencies are closely related to the Ag^+ dose released in the microbial microenvironment.[41] Therefore, developing infection-responsive silver complexes with high Ag^+ contents that are below the toxic limit is crucial to improve antimicrobial effects while minimizing toxic side-effects and resource waste. Herein, stimuli-responsive composites were fabricated by decorating HA or Fe(III)–TA complexes on a Ag(I) complex with high Ag^+ content to achieve on-demand HAase or pH-responsive antimicrobial performance (Scheme 1). Ag(I) complex (**1**) acted as an effective antimicrobial agent, and infection microenvironment cues, *i.e.* hyaluronidase (HAase) and acidity, were used as feasible endogenous triggers for target-specific Ag^+ release from **1**. Stimuli-responsive degradation of the coatings was realized through HAase-induced hydrolysis of HA and pH-sensitive cleavage of the coordination bonds of Fe(III)–TA, respectively. Under neutral physiological conditions, the Ag(I) complex was encapsulated within HA or Fe(III)–TA coatings, and Ag^+ leaching was efficiently inhibited. In an infection microenvironment, HA and Fe(III)–TA coatings were disrupted in response to HAase or acid secreted by bacteria, leading to exposure of the incorporated Ag(I) complex. The exposed Ag(I) complex could eliminate bacteria attached to the surface first and then eradicate bacteria in solution by releasing Ag ions sustainably.

To achieve efficient microbial eradication, the design of the ligands is crucial. AgC≡C^{t}Bu was selected because it displays a special ability for constructing Ag clusters with high silver content, with silver nuclear numbers from 3 through 12[43,44] to even 70[45] due to the linear geometry of the alkynyl unit,[46] facilitating the formation of silver clusters assembled with Ag···Ag metallophilic interactions.[47,48] Biocompatible *p*-phenyldiacetonitrile (*p*-phda) was employed as a bridging ligand because its hard base character promotes the coordination with soft acid Ag(I) ions to form a complex with moderate stability, favouring sustained release of Ag^+. It is noted that in previously published stimuli-responsive platforms, metal complexes were generally employed as carrier vehicles (hosts) for antimicrobial drugs[31,49–51] by utilizing their distinct attributes, such as well-defined pore sizes and high loading capacity. In the current system design, the Ag(I) complex behaves as both a carrier and an antibacterial drug because the Ag ions form the node of the carrier. This design strategy can avoid the use of an additional carrier for the antimicrobial agents, thereby reducing cost and the side effects of degradation in the infection microenvironment. A number of characterizations, including FT-IR spectroscopy, single-crystal X-ray diffraction analysis, thermogravimetric analysis, UV spectroscopy, contact angle testing, zeta potential, SEM, dynamic light scattering (DLS), and Ag^+

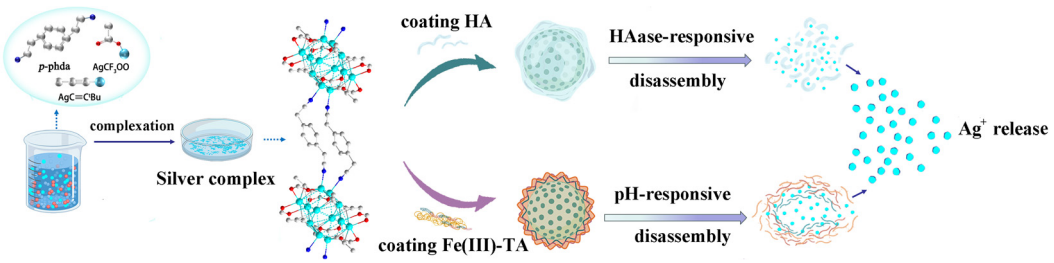

Scheme 1 Schematic of this work.

release studies, inhibition zone measurements, and minimal inhibition concentration (MIC) determinations were conducted to elucidate (1) the crystal structure of the Ag(I) complex, (2) the relationship between Ag^+ content and Ag^+ release, (3) the stimulus-responsive degradation of HA and Fe (III)–TA coatings, and (4) the stimulus-triggered Ag^+ release and antimicrobial performance of the composites.

Experimental

Materials and methods

Unless otherwise indicated, all starting materials were obtained from commercial suppliers and used as received without further purification. Infrared spectra were recorded as KBr disks with an FT-IR-8900 (BRUKER). UV–vis spectra were recorded with a JASCO V-550 spectrometer. Elemental analyses were performed with a VarolEL III (Elementar) elemental analyser. X-ray powder diffractions were conducted on an XRD-7000 diffractometer (SHIMADZU). Thermogravimetric analyses were recorded on a WRT-3P microthermal balance (Shanghai Precision Instrument Company). Static contact angles were investigated by advancing or receding *ca.* 2 μL of deionized water using a syringe onto the sample surface, and the drop was measured with an automated contact angle analyser with a goniometer (SDC 100, SINDIN). The errors of the contact angle measurements are ±1°. At least six measurements were performed on each surface. SEM imaging was performed with a VEGA3 (TESCAN) by solution casting. The hydrodynamic particle size and zeta potential were determined by DLS with a laser particle size analyser (DelsaMax Pro, Beckman Coulter). Silver ion release was measured with a ZEEnit 700 P atomic absorption spectrometer (Analytik Jena AG). The optical density at 450 nm and 660 nm (OD600) was measured with an EPOCH2 microplate reader (BioTek).

X-ray crystallography

A selected single crystal of **1** was used for data collection with a Bruker SMART APEX-II CCD diffractometer using the multi-scan technique at 150 K with Cu-Kα radiation (λ = 0.154184 Å). A total of 16 455 reflections were collected, and 7203 reflections were used for refinement. The linear absorption coefficient was 3.823. The structure was solved with ShelXL refinement package[52] using least-squares minimization and refined with Olex2.[53] The refinement suffered from high residual peaks/electron density near the metal sites, resulting in high *R* values.

Synthesis of $AgC{\equiv}C^tBu$

$AgC{\equiv}C^tBu$ was synthesized by following a previously reported protocol.[54] Briefly, $AgNO_3$ (1.0450 g, 15 mmol) was added to a three-necked flask and dissolved in acetonitrile (70 mL). After stirring thoroughly, $HC{\equiv}C^tBu$ (2.4 mL) and triethylamine (2.6 mL) were added, and the reaction was stirred for an additional 48 h at room temperature. The resulting precipitates were filtered out and washed 3 times with acetonitrile. After drying at 70 °C, a white powder was obtained. Yield: 83.15% (0.8960 g, based on $AgNO_3$). IR (KBr, ν/cm^{-1}): 2962(s), 2862(s), 2052(w), 1450(s), 1242(m).

Synthesis of $[Ag_{12}(C{\equiv}C^tBu)_6(CF_3COO)_6(p\text{-phda})_2]_n$ (1)

Complex **1** was prepared by mixing $AgC{\equiv}C^tBu$ (0.1211 g, 0.6 mmol), $AgCF_3COO$ (0.2214 g, 1 mmol) and *p*-phda (0.1990 g, 1 mmol) in methanol (10 mL). After stirring for 30 min, ethanol (12 mL) was added to the resultant bright-yellow solution, which was then introduced into a 9 mm diameter glass tube. Colourless crystals of **1** suitable for single-crystal X-ray analysis were obtained by slow evaporation at room temperature. Yield: 30.14% (0.0600 g, based on *p*-phda). Anal. Calcd for $C_{34}H_{35}N_2O_6F_9Ag_6$ C, 19.44; N, 2.02; H, 2.51%; Found: C, 19.15; N, 2.31; H, 2.31%. IR (KBr, ν/cm^{-1}): 2961(s), 2862(s), 2245(m), 2005(w), 1967(s), 1519(m), 1427(m), 1357(m), 1203(s), 1134(s), 840(m), 802(m), 725(s). Rapid synthesis of complex **1** was accomplished according to the referenced method,[55] and the phase purity was verified by PXRD (Fig. S1).

Synthesis of 1@HA

Mass ratios of **1** : HA of 2 : 1, 1 : 1 and 1 : 2 were used to optimize the preparation of **1**@HA; the resulting composites were labelled as **1**@HA (2 : 1), **1**@HA (1 : 1) and **1**@HA (1 : 2), respectively. Complex **1** (0.0100 g, 0.0500 mmol) was added to 10 mL of an aqueous solution of HA (0.0050, 0.0100 and 0.0200 g, respectively) at room temperature. After stirring for 30 min followed by sonicating for 30 min, **1**@HA was obtained by centrifugation (3000 rpm for 15 min).

Synthesis of 1@Fe(III)–TA

3 mL of an aqueous solution of TA (0.0100 g) and $FeCl_3{\cdot}6H_2O$ (0.0030 g) was added to an aqueous solution of **1** (0.0693 g, 0.0500 mmol) (pH 8). The resulting **1**@Fe(III)–TA was purified by centrifugation (3000 rpm for 15 min) and washed 3 times with water to remove the excess of unreacted substances.

Antimicrobial tests

The antimicrobial activities of the compounds were trialled against *Staphylococcus aureus* (CGMCC 1.2910), *Pseudomonas aeruginosa* (CGMCC 1.2814), carbapenem-resistant *Escherichia coli* (BW25113 (NDM-1)) and *Candida albicans* (CGMCC 2.2086) by using inhibition zones, minimal inhibitory concentrations (MICs) and growth inhibition assays. All routine handling of bacteria was performed using standard antimicrobial methods for bacteria and yeast, as published by CISI.[56,57] Complex **1** (1024 mg L^{-1}) was suspended in different medium and DMSO (1%), and the effective dose was obtained by two-fold dilution for antimicrobial testing.[58]

Zone of inhibition technique

The well-diffusion method[59] was used for antibiotic susceptibility testing. The turbidity of the medium (which included the above-mentioned) was adjusted to 10^6 CFU mL^{-1} and spread evenly over the surface of the agar plate. Subsequently, each medium was drilled with four holes (diameter of 6 mm), and

20 μL of antibacterial sample (1000 mg L^{-1}) was added to each hole.[60] After storing in a biochemical incubator at 37 °C for 18 h, the diameters of the inhibition zones were measured with vernier calipers.

Minimal inhibition concentration (MIC)

Continuous dilutions of **1**, **1**@HA and **1**@Fe(III)–TA (32 to 256 mg L^{-1}, with or without the culture medium containing 1 wt% HAase or with pH 5.5) were prepared in a 96-well plate, and bacterial inoculum (10^6 CFU mL^{-1}) was added to each well. After incubation for 18–24 h at 37 °C for carbapenem-resistant *E. coli*, *P. aeruginosa* and *S. aureus* and at 30 °C for *C. albicans*, the optical densities at 660 nm were measured, and the MICs were determined. Broth containing bacteria alone was used as a blank control. The microbial growth in acidic conditions (pH 5.5) or in the presence of HAase was examined and was not affected.

Growth inhibition assay

The serial dilution solution of **1** (16 to 256 mg L^{-1}) was added to diluted bacteria cultures (10^6–10^7 CFU mL^{-1}) in 96-well plates and incubated at 37 °C for 48 h. The OD600 was measured for all samples every 2 h in the first 12 h and then every 12 h to construct growth curves for the bacteria. A sample containing only broth was used as the blank control.

Silver release

The samples of **1**, **1**@HA and **1**@Fe(III)–TA PBS aqueous solution (100 μL mL^{-1}) before and after treatment with pH 7.4, 1 wt% HAase or pH 5.5 were suspended in physiological buffers and stirred vigorously. The supernatant fluids of suspensions of different immersion times were sampled, diluted, and quantified by atomic absorption spectroscopy to determine the Ag^+ concentrations. The release ratio of **1** was calculated from the released Ag^+ mass divided by the Ag^+ content in **1**. The release ratios of **1**@HA or **1**@Fe(III)–TA were calculated with the released Ag^+ mass divided by the mass of **1**@HA or **1**@Fe(III)–TA, respectively.

Cell viability

The *in vitro* cytotoxicity of **1** was evaluated using Human Kidney 2 cells (HK-2) and determined with a Cell Counting Kit-8 (CCK-8) assay, at doses ranging from 8 to 256 mg L^{-1}. HK-2 cells were seeded in 96-well plates and cultured in high-glucose DMEM containing 1% streptomycin, 1% penicillin, and 10% heat-inactivated FBS at 37 °C in a humidified incubator (5% CO_2) for 24 h, followed by exposure to various concentrations of DMSO solutions of **1** for 24 h. Subsequently, 10 μL of CCK-8 was added to each well and incubated for an additional 1 h at 37 °C. Cell viability was determined by measuring the optical density at 450 nm using an EPOCH2 microplate reader (BioTek). Cell viability was calculated according to the following equation: CV (%) = [(OD of treated cells − OD of blank cells)/(OD of vehicle control cells − OD of blank cells)] × 100%. A 1% DMSO solution was used as a vehicle control, and 10% DMSO solution was used as a positive control.

Statistical analyses

Where appropriate, the data are presented as means with standard deviations (SD) as error bars, calculated from measurements performed in triplicate in three independent experiments.

Results and discussion

Infrared spectra analysis of 1

The FT-IR spectra of AgC≡C^{t}Bu and **1** are illustrated in Fig. S2. The spectrum of **1** showed bands at 2245 cm^{-1} and 2005 cm^{-1}, corresponding to the typical ν_s(C≡N) of *p*-phda (2249 cm^{-1}) and ν_s(C≡C) of AgC≡C^{t}Bu (2052 cm^{-1}). The shifts of the C≡N (+4 cm^{-1}) were considered to arise from the contribution of a π-back-donation effect of the cyano group,[42] indicating *p*-phda was involved in the coordination. Besides, typical ν_s(C=O) and ν_s(C–F) peaks of CF_3COO^- anions appeared at 1697 cm^{-1}, 1203 cm^{-1}, and 1134 cm^{-1}, evidencing the incorporation of anions. All the above information indicated *p*-phda, AgC≡C^{t}Bu and CF_3COO^- are all included in **1**.

Crystal structure of 1

The crystal structure of **1** was determined by single-crystal X-ray crystallographic analysis, with crystallographic data presented in Table S1 and selected bond distances listed in Table S2. Complex **1** is revealed as a 1D chain assembled from Ag_{12} clusters with bridging *p*-phda ligands (Fig. 1a). Twelve silver ions are held together by coordination with six $[C{\equiv}C^tBu]^-$ ligands and six CF_3COO^- anions forming the Ag_{12} cluster. The $[C{\equiv}C^tBu]^-$ ligands adopt μ_4-η_1,η_1,η_1,η_1 and μ_4-η_1,η_1,η_1,η_2 connecting modes (Fig. 1b), while CF_3COO^- exhibits chelating coordination to the Ag centres. The cage-like Ag_{12} clusters contain three quadrilateral Ag_4 units (Ag1-Ag6-Ag5-Ag3, Ag2-Ag4-Ag2a-Ag4a and Ag1a-Ag3a-Ag5a-Ag6a), which are parallel each other (Fig. 1c). In the Ag_{12} cage, the Ag···Ag distances of Ag4/4a-Ag6 (2.8520(19) Å) and Ag4a-Ag5/5a (2.8670 (19) Å) are shorter than the covalent radii of two silver atoms (2.88 Å) and are defined as Ag–Ag bonds. The other Ag···Ag distances are in the range of 2.921(19) Å–3.380(21) Å, which are shorter than twice the van der Waals radius of silver (3.44 Å), thus being considered as strong Ag···Ag interactions. The silver ion content of **1** is as high as 46.76%, which is significantly higher than the previous results (13.46%–16.29%,[41] 28.50%–30.67%[42] and 39.57%[61]). As expected, the rational employment of AgC≡C^{t}Bu achieved a complex with high silver content.

Thermal stability of 1

The TG curve of **1** showed two major weight losses (Fig. S3). The first weight loss of 40.13% occurs from 99 °C to 276 °C, corresponding to liberation of $[C{\equiv}C^tBu]^-$ and $[CF_3COO]^-$ (calcd. 40.70%). Further rapid weight loss of 22.07% occurs in

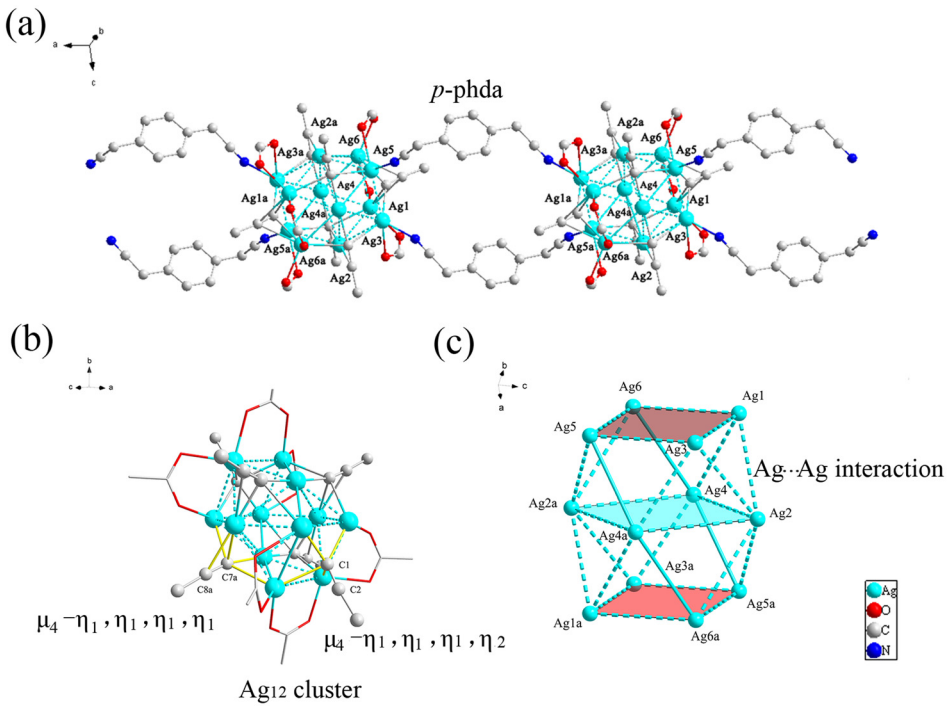

Fig. 1 Crystal structure of **1** showing the polymeric chain (a), Ag_{12} cluster (b), and silver cage (c). Hydrogen and fluorine atoms are omitted for charity. Symmetric code a: 2 − *x*, 1 − *y*, 1 − *z*.

the range 350 °C to 420 °C, which is attributed to the removal of *p*-phda (calcd. 22.51%) to give an amorphous residue.

1@HA

A satisfactory HA coating should be able to effectively suppress silver ion release under normal physiological conditions while enabling a sensitive HAase-responsive decomposition under infection conditions. Therefore, the mass ratio of **1**/HA is crucial and was optimized by combined evaluation of the release of silver ions before and after treatment of the coating with HAase (Fig. 2a). **1** : HA ratios of 2 : 1, 1 : 1 and 1 : 2 (w/w) were employed in the fabrication of **1**@HA. Ag^+ release results showed that **1**@HA (1 : 2) exhibited the optimal Ag^+ release inhibition (3.55%) yet the poorest responsive sensitivity with the lowest Ag^+ release ratio of 23.92%. **1**@HA(2 : 1) exhibited the highest Ag^+ release (19.50%) and comparable responsive Ag^+ release (58.47%) after treatment. **1**@HA (1 : 1) achieved an ideal combination, with moderate Ag^+ leakage (14.99%) under normal physiological conditions and the highest HAase-triggered Ag^+ release (59.26%). These results suggested the optimal mass ratio of **1** and HA is 1 : 1. Contact angle measurements also supported the above optimization (Fig. 2a). The water contact angle for **1** is 150.74°, which suggests its hydrophobicity. After coating with HA, the water contact angles of **1**@HA (2 : 1), **1**@HA (1 : 1) and **1**@HA (1 : 2) reduced to 63.66°, 29.74° and 17.35°, respectively, due to the formation of hydrogen bonds. The smaller the contact angle, the more complete the HA coating. Upon treatment with HAase (1 wt%), the contact angles of these composites increased to 117.71°, 127.98° and 73.08°, respectively, indicating the decomposition of the hydrophilic HA coating to varying degrees. Consistent with the Ag^+ release analysis, **1**@HA (1 : 1) displayed mild hydrophilicity with a moderate water contact angle coupled with the highest hydrophobicity, originating from the exhaustive disassembly of the HA coating. Therefore, **1**@HA (1 : 1) was selected for further investigations and hereafter referred to as **1**@HA.

In addition to the above confirmation of HA coating from changes in the water contact angles and Ag^+ release, the successful coating of HA on **1** for **1**@HA was further characterized by FT-IR, zeta potential, SEM, and DLS examination. As anticipated, the FT-IR spectrum of **1**@HA showed the characteristic anti-symmetric out-of-plane ring stretch of the sugar group (923 cm^{-1}) and stretching vibration peaks for the C–O–C of HA (1180 cm^{-1}), indicating HA was coated on **1** (Fig. 2b). However, ν_s(O–H) (3325 cm^{-1} for HA) shifts to a high-frequency region (3448 cm^{-1}) attributed to coordination of unsaturated Ag^+ with –OH upon HA modification.[62] The inversion of the zeta potential of **1**@HA from +5.05 mV for **1** to −14.27 mV provided further evidence of successful coating of HA on **1**, which originates from the negatively charged HA (Fig. 2c).[63] SEM images, assisted by particle size statistical analysis, provided visual proof of the successful coating (Fig. 2d). The prepared silver complex **1** showed irregular spherical shapes with average particle sizes of approximately 0.68 μm. HA wrapping caused morphological changes and a slight increase in the average particle size, reflecting the effect of the coating. The hydrodynamic particle size of **1** and **1**@HA determined by DLS (intensity-

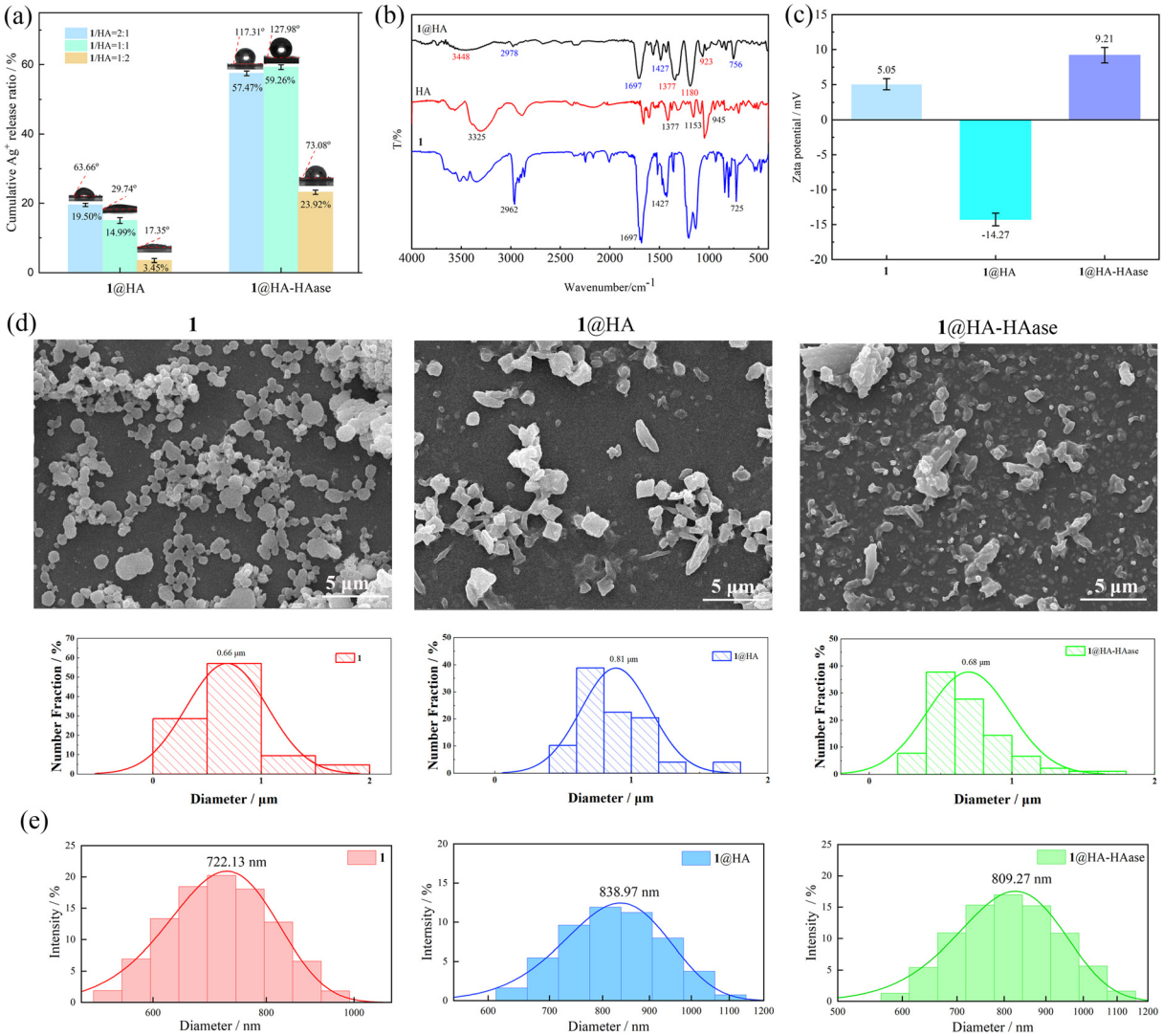

Fig. 2 Characterization of **1**@HA. (a) Optimization of **1**/HA ratios with respect to Ag^+ release and water contact angles, (b) IR spectra, (c) zeta potential, (d) SEM images with particle size analysis, and (e) DLS analysis.

weighted) was 722.13 nm and 838.97nm, respectively (Fig. 2e). The hydrodynamic diameter of **1** measured by DLS was larger than that determined by analysis of the SEM images, which is attributed to the contribution of the hydration layer of particles in solution to particle sizes during DLS analysis as well as to shrinkage of particles during SEM measurements.

1@Fe(III)–TA

The coating effects of the Fe(III)–TA complex on **1** were evaluated by Ag^+ release. The Ag^+ release ratio of **1**@Fe(III)–TA was successfully restrained to 3.31% in PBS with pH 7.4 and increased to 23.92% in PBS at pH 5.5, indicating the successful coating of the Fe(III)–TA complex on **1** (Fig. 3a). Considering the moderated pH-responsive Ag^+ release of 23.92%, perhaps due to the thicker coating, less mass of $FeCl_3{\cdot}6H_2O$ and TA was employed to prepare **1**@Fe(III)–TA with thinner coatings for elevated Ag^+ release. However, the change in the pH-responsive Ag^+ release (24.25%) was not significant, while the Ag^+ release ratio under normal conditions increased to 4.80%. Therefore, the optimal Fe(III)–TA decoration was determined as that of the originally described experiment.

The combined FT-IR, UV, zeta potential, SEM, EDAX mapping and DLS analyses characterized the expected coating of the Fe(III)–TA complex on **1**. In the FT-IR spectrum of **1**@Fe(III)–TA, the ν_s(C=C) and ν_s(C=O) peaks assigned to TA were observed around 1570 cm^{-1} and 1718 cm^{-1}, respectively, indicating the incorporation of TA (1533 cm^{-1} and 1718 cm^{-1} for free TA). The broad peak of ν_s(O–H) at 3500 cm^{-1} for free TA shifted to 3458 cm^{-1}, indicating that the -OH groups of TA are coordinated with Fe^{3+} (Fig. 3b).[64] In UV-Vis spectra, newly appearing absorptions at 204 nm, 346 nm, and 433 nm were assigned to the intrinsic $\pi \rightarrow \pi^*$ transition of TA, charge transfer from ligand to metal (LMCT) in Fe(III)–TA complex,[65] and d-d transition of Fe^{3+}, respectively (Fig. 3c).[66] Inversion of the zeta potential of **1**@ Fe(III)–TA from +5.05 mV for **1** to −19.50 mV provided added evidence for Fe(III)–TA complex dec-

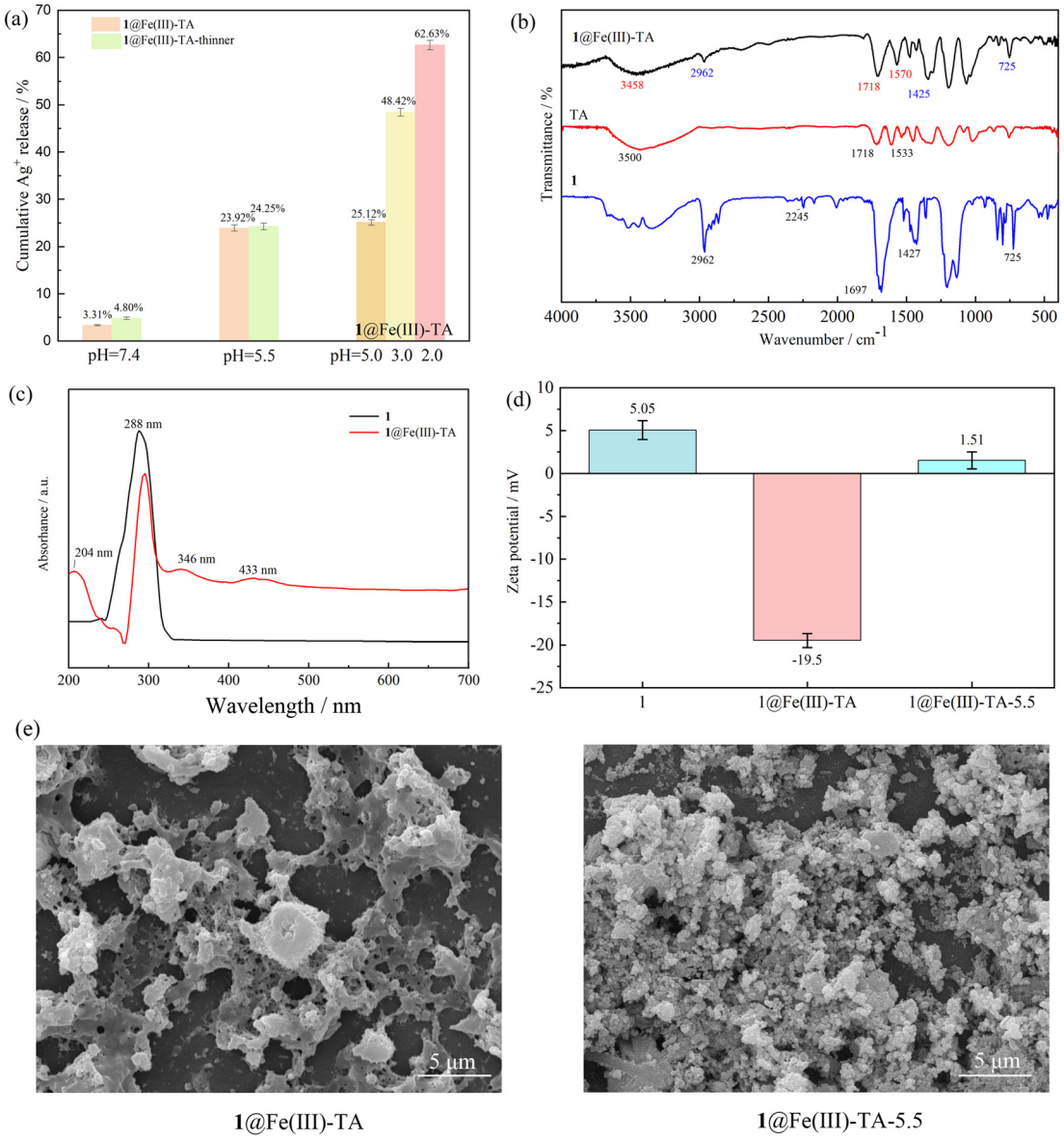

Fig. 3 Characterizations of **1**@Fe(III)–TA before and after treatment with acid. (a) Optimization of **1**@Fe(III)–TA with respect to Ag^+ release, (b) IR spectra, (c) UV-Vis spectra, (d) zeta potential, and (e) SEM images.

oration on **1** (Fig. 3d). SEM imaging revealed that particles of **1** presented extensive agglomeration and adhesion upon modification with the Fe(III)–TA complex (Fig. 3e). The hydrodynamic particle size displayed two distributions, corresponding to non-agglomerated particles and aggregates (Fig. S4a). Finally, EDAX mapping results for the elemental distribution revealed that Fe components are distributed evenly in the samples (Fig. S4b). All the above results demonstrated clearly that **1** was coated uniformly with the Fe(III)–TA complexes.

Responsive properties

The HAase-response of **1**@HA and pH-response of **1**@Fe(III)–TA were examined by zeta potential measurements. After incubation of **1**@HA with HAase, its zeta potential was inverted from −14.27 mV to +9.21 mV, demonstrating its response to HAase, which is attributed to exposure of the inherently positively charged **1** after HA film dissolution (Fig. 2c). In normal PBS at pH 7.4, the zeta potential of **1**@Fe(III)–TA is −19.5 mV due to the -OH groups of TA (Fig. 3d). However, the value reverted to +1.51 mV after treatment with acid to pH 5.5, clearly indicating the designed pH-sensitivity of the Fe(III)–TA film. The HAase response of **1**@HA and the pH response of **1**@Fe(III)–TA were also evidenced visually by contact angle (Fig. 2a) and/or SEM images (Fig. 2d and 3e). Treatment with HAase for **1**@HA led to wettability recovery from hydrophilicity to hydrophobicity as well as obvious morphological changes with a decrease in particle size. **1**@Fe(III)–TA also exhibited acid-triggered morphological transformations. Their stimulus-

responsive performances were verified further by studying Ag^+ release, as discussed in detail in the section on Ag^+ release.

Antimicrobial performance of 1

To evaluate the antimicrobial activity of **1**, different strains, including Gram-positive bacteria (*S. aureus*), Gram-negative bacteria (*P. aeruginosa* and carbapenem-resistant *E. coli*), and yeast (*C. albicans*) were used as model microorganisms, and $AgNO_3$ ointment and cefazolin were selected as controls. The inhibition zones of **1** for the four strains are displayed in Fig. 4 and Table S3. **1** exhibited antimicrobial activities with a wide-spectrum action against all four strains. It showed effective activities against *C. albicans* and *P. aeruginosa* (16.85 mm and 14.21 mm, respectively), as well as moderate activities against the other two strains (10.01 mm for *S. aureus* and 10.89 mm for carbapenem-resistant *E. coli*). In contrast, cefazolin displayed stronger antibacterial activities against *S. aureus* and carbapenem-resistant *E. coli*, with inhibition-zone diameters of 29.81 mm and 12.84 mm, respectively, as well as weaker activities against *C. albicans* and *P. aeruginosa*, with inhibition-zone diameters of 8.25 mm and 9.83 mm, respectively. These selective antimicrobial activities demonstrated the limited efficiency of the antibiotic action against fungi and drug-resistant bacteria. $AgNO_3$ ointment showed the lowest antimicrobial activity against all four bacteria because of the lower content of silver ions (0.1 wt%). Because the inhibition zone is a semi-quantitative evaluation with limited precision, further studies to determine the MIC values of **1** against the four strains were conducted to quantify their antimicrobial activities; the results are presented in Table S4.

1 exhibited the lowest MIC against *C. albicans* (32 mg L^{-1}), and the values for the other three bacteria were all 128 mg L^{-1}. The MICs of **1** were further expressed in the final concentration of silver ion (hereafter referred to as AgMICs) because the nature of its antibacterial activities is determined by the silver ion content. The AgMICs of **1** are 1.39×10^{-5} mol Ag per L for *C. albicans* and 5.54×10^{-5} mol Ag per L for the other three bacteria. **1** showed the best antimicrobial effect against *C. albicans* due to its slower growth cycle than the other three bacteria, which was consistent with the corresponding largest inhibition-zone diameter. In comparison with our previous results, **1** exhibits better antibacterial activities than {[Ag_2(1,5-

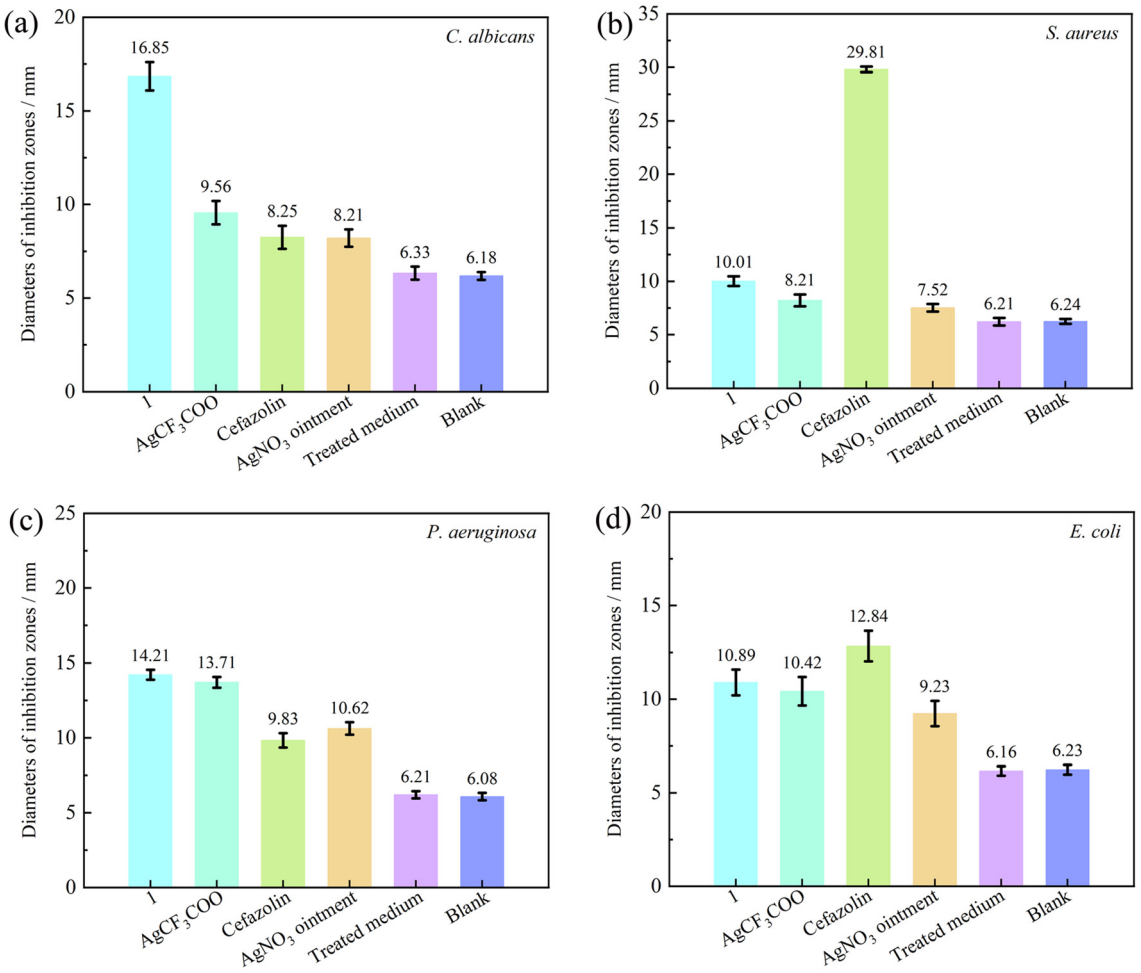

Fig. 4 Inhibition zones of **1**, cefazolin, and $AgNO_3$ ointment for *C. albicans* (a), *S. aureus* (b), *P. aeruginosa* (c), and carbapenem-resistant *E. coli* (d). Treated medium: HAase (1 wt%) and pH 5.5.

nds)(DMSO)$_2$]DMSO}$_n$ (8.15–10.86 × 10^{-5} mol Ag per L), {[Ag(*p*-phda)$_2$](BF$_4$)}$_n$ [42] (5.92–7.89 × 10^{-5} mol Ag per L) and [Ag$_2$(CF$_3$COO)$_2$(1,4-dcb)(C$_8$H$_{10}$)]·2ofbp·H$_2$O [41] (6.74–8.86 × 10^{-5}mol Ag per L). These results suggest that the construction of a high-silver-content complex is an effective approach to improve antimicrobial activities.

It is interesting that **1** showed excellent inhibition of antibiotic-resistant *P. aeruginosa* and carbapenem-resistant *E. coli*. Therefore, the growth of the two bacteria in the presence of different concentrations of **1** was further investigated (Fig. 5). At 32 mg L^{-1}, 1 achieved complete suppression of *P. aeruginosa* growth within 4 h, whereas at 64 mg L^{-1}, it extended the lag phase of carbapenem-resistant *E. coli* to 7 h. In the presence of 128 mg L^{-1} of **1**, the growth of both bacteria was inhibited thoroughly within 50 h, which indicated its effective and sustained antimicrobial abilities. It is worth noting that, after 24 hours, **1** (32–64 mg L^{-1}) exhibited inhibition effects on *P. aeruginosa*, as evidenced by the decreased OD values. This result is especially encouraging and demonstrates the merits of long-term and slow release of **1**.

Responsive antimicrobial performance of 1@HA and 1@Fe(III)–TA

It has been well-illustrated that intense bacterial metabolic activities result in local hypoxia, which, in turn, leads to slight acidity (pH 4.5–6.5) and high expression of enzymes (HAase) in the infection environment.[67,68] Therefore, the HAase/pH-responsive performances of the two composites were further studied by examining the inhibition zones and MICs. The pH value was adjusted to 5.5 (the average of 4.5 and 6.5). The diameters of the inhibition zones of the blank in the treated medium for all strains are almost the same as those of the blank in normal PBS, suggesting the negligible influence of the treated medium on the growth of all strains.

In non-stimulus environments, the inhibition-zone diameters for **1**@HA are 10.32 mm, 10.23 mm, 9.56 mm and 12.12 mm for *P. aeruginosa*, *C. albicans*, carbapenem-resistant *E. coli*, and *S. aureus*, respectively (Table S5); the MICs of **1**@HA for the four strains were 128 mg L^{-1}, 512 mg L^{-1}, 64 mg L^{-1} and 256 mg L^{-1}, respectively (Table S6). In the presence of HAase, the inhibition-zone diameters of HAase-treated **1**@HA increased from 10.32 mm to 14.56 mm (+4.24 mm) for *P. aeruginosa*, from 10.23 mm to 10.86 mm (+0.63 mm) for *C. albicans*, and from 9.56 mm to 11.45 mm (+1.89 mm) for carbapenem-resistant *E. coli*, which indicated that HAase could degrade HA and facilitate on-demand Ag$^+$ release. One exception was for *S. aureus*, for which the inhibition zone diameter decreased from 12.12 mm to 11.83 mm (−0.29 mm), probably due to uneven spreading of the medium and experimental error. The MICs of **1**@HA decreased from 128 mg L^{-1} to 64 mg L^{-1} for carbapenem-resistant *E. coli* and from 512 mg L^{-1} to 64 mg L^{-1} for *C. albicans*. MICs of **1**@HA for *P. aeruginosa* and *S. aureus* remained unchanged, probably due to the insignificant response triggered by 1 wt% HAase. The inhibition-zone diameters and MICs shown by the above results proved the potential of **1**@HA for enzyme-responsive on-demand antimicrobial applications.

Similarly, **1**@Fe(III)–TA showed pH-responsive abilities, as evidenced by the increase in the inhibition zones and a decrease in the MICs. At pH 5.5, the inhibition-zone diameters was enlarged by 0.1 mm for *C. albicans* (from 11.10 mm to 11.20 mm) compared to **1**@Fe(III)–TA at pH 7.4, whereas for *P. aeruginosa* the value showed a significant increase of +5.70 mm (from 9.56 mm to 15.26 mm) and +1.98 mm for carbapenem-resistant *E. coli* (from 10.23 mm to 12.21 mm) (Table S5). This is because *P. aeruginosa* and carbapenem-resistant *E. coli* could generate larger amounts of acid than *C. albicans*, leading to lower pH at the infected sites. The phenomenon is interesting and demonstrates the superior acid-triggered degradation of **1**@Fe(III)–TA for acid-producing bacteria. In addition, the MICs of **1**@Fe(III)–TA at pH 5.5 are 256–512 mg L^{-1} for the four strains and are lower than those at pH 7.4 (1024 mg L^{-1}, Table S6).

Ag$^+$ release

The antimicrobial activities of Ag(I) complexes are governed by released Ag$^+$ quantities[69,70] and the extent of ligand displace-

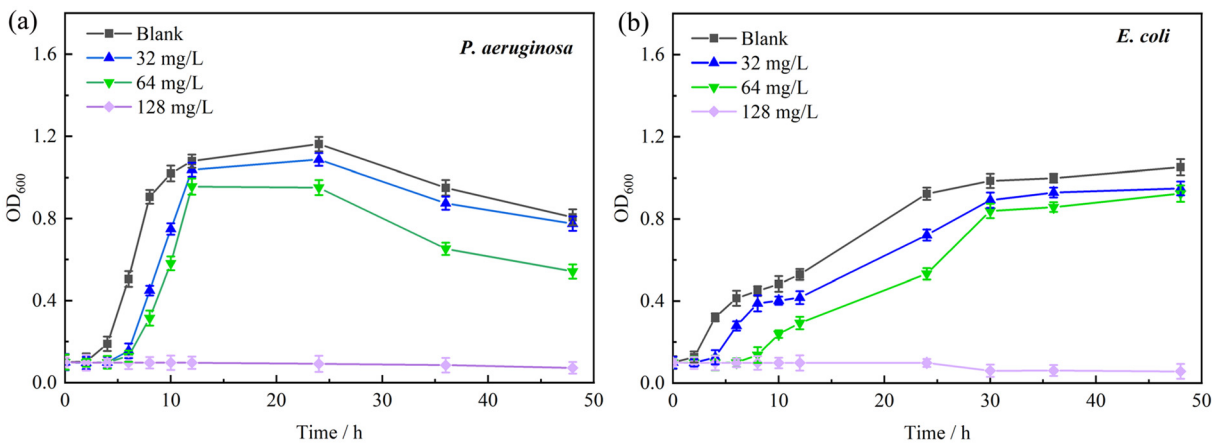

Fig. 5 Growth curves of (a) *P. aeruginosa* and (b) carbapenem-resistant *E. coli* in different concentrations of **1**.

ment by bacterial components.[41] The Ag^+ content of **1** is 46.76%, which is much higher than those of our previously published structures.[41,42] However, high Ag^+ content in the complex does not always mean high Ag^+ release in solution. Therefore, the amount of Ag^+ released from **1** and the two composites was measured by suspending them in PBS buffer with the same initial concentration of 100 mg L^{-1} (Fig. 6(a)).

For **1**, Ag^+ concentrations increased linearly within 4 h and then slowly reached a plateau and remained at 23.50 mg L^{-1} for the subsequent 2 days. This result indicated that **1** could give a steady and prolonged release of Ag^+. The Ag^+ release ratio was calculated to be 50.79%, which is higher than the 43.82% release ratio reported in the previous study,[41] yet lower than that of $\{[Ag(p\text{-phda})_2](BF_4)\}_n$ (72.59%).[42] The 2.22 g cm^{-3} density of **1** is significantly larger than those of the reported structures (1.55–2.04 g cm^{-3}),[42] suggesting its compact packing. The crystal structure revealed that **1** is assembled as a chain of Ag–N, Ag–O, and Ag–C coordination bonds, as well as extensive Ag–Ag bonds and Ag···Ag interactions. These bonds and interactions inhibited the dissolution of Ag^+ to a certain degree and resulted in a lower Ag^+ release ratio.[42] Although the original Ag^+ content is increased greatly by the smart choice of using AgC≡C^{t}Bu as a ligand, its contribution to the antibacterial efficiency was meanwhile partially offset by the generated compact structure assembled through extensive interactions. These interpretations indicate that it is crucial to keep a balance between increased Ag^+ content, while maintaining a loose packing structure. Nevertheless, the Ag^+ concentration of 23.5 mg L^{-1} for **1** is still larger than those of our previous results (2.52–15.49 mg L^{-1}).[41,42]

Subsequently, the HAase-responsive Ag^+ release of **1**@HA was examined. As shown in Fig. 6(a), in the absence of HAase, the Ag^+ release ratio of **1**@HA after 3 days is 14.99%, which is much lower than for **1** (50.79%). Coating with HA achieved the suppression of Ag^+ leaching, although not outright prevention. However, in the presence of 1 wt% HAase, the value increased sharply to 59.26%, revealing clearly the HAase-switched Ag^+ release under infection conditions. These results are also consistent with the increase in the inhibition zone and the reduction of AgMIC for **1**@HA in the presence of HAase. Therefore, **1**@HA exhibits effective and controlled Ag^+ release triggered by HAase, which allows it to specifically exert antimicrobial effects within the infected sites while minimizing damage to surrounding healthy tissues due to premature leakage.

The pH-sensitive Ag^+ release of **1**@Fe(III)–TA is shown in Fig. 6(b). At pH 7.4, the Ag^+ release ratio is 3.31%, which is a marked absolute decrease of 47.48% compared to that of **1** (50.79%). The negligible Ag^+ release demonstrated the effective coating of Fe(III)–TA, in accord with the inversion of zeta potential and SEM mapping results of **1**@Fe(III)–TA (section 3.2.2). At pH 5.5, the Ag^+ release ratio increased from 3.31% to 23.92%, indicating a clear pH-dependent acceleration of Ag^+ release originating from the disassembly of Fe(III)–TA coating in response to acidity. The lower silver release ratio of **1**@Fe(III)–TA at pH 5.5 can be used to further explain the negligible increase in the inhibition-zone diameter against *C. albicans* (section 3.5). Since the negligible degree of Ag^+ release and SEM results of **1**@Fe(III)–TA confirmed the complete coating of Fe(III)–TA on **1**, the lower pH-responsive Ag^+ release ratio can reasonably be attributed to the less effective cleavage of coordination bonds of Fe(III)–TA at pH 5.5. In other words, only partial coordination bonds between the OH groups of TA and Fe^{3+} were cleaved, leading to less effective Ag^+ release (Scheme S1).[70] The observed lower zeta potential of 1.51 mV for **1**@Fe(III)–TA after treatment than that for **1** (5.05 mV) provided experimental evidence for incomplete disassembly of the Fe(III)–TA coating at pH 5.5. Further, pH-dependent Ag^+ release was performed to clarify the proposed pH-dependent decomposition of Fe(III)–TA (Fig. 3a). The results verified that the Ag^+ release ratio increased monotonically with acidity. When the acidity was elevated from pH 5 to 2, the Ag^+ release ratio increased considerably from 25.12% to 62.63%. Therefore, based on the above results and interpretations of the acid-responsive antibacterial activity, **1**@Fe(III)–TA is more suitable for killing high-metabolism Gram-negative bacteria with stronger acid-production (*i.e. P. aeruginosa* and carbapenem-resistant *E. coli*).

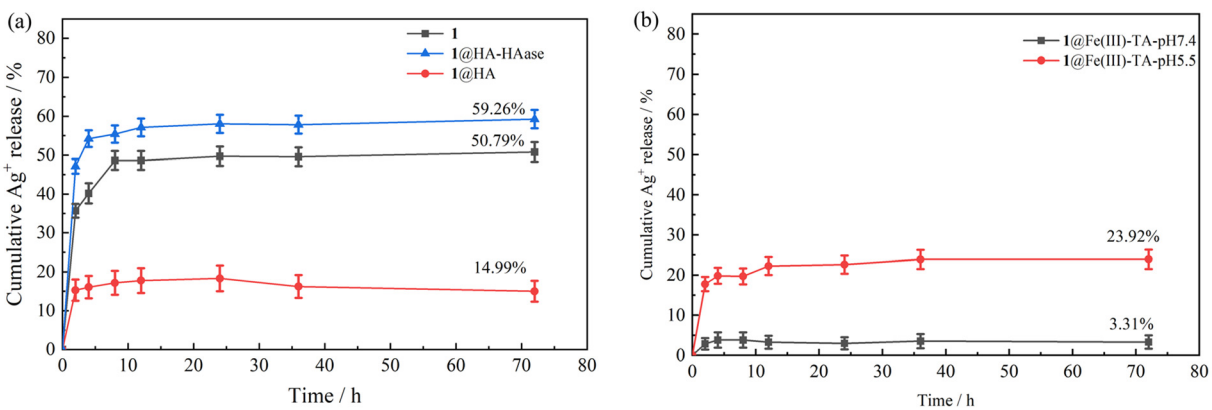

Fig. 6 Ag^+ release ratio as a function of time for **1**, **1**@HA (a), and **1**@Fe(III)–TA (b) before and after treatment with HAase or pH 5.5.

In vitro biocompatibility

Another key point concerns the *in vitro* biocompatibility of the Ag complex as an antimicrobial agent in practical clinical applications. It is reported that possible physical damage by the Ag complex to bacterial cells did not induce *in vitro* cytotoxicity, even at high doses of 220 mg kg^{-1}.[71] The largest AgMIC for the current silver complex for the tested strains is 5.98 mg Ag per L (5.54×10^{-5} mol Ag per L), demonstrating its potential *in vitro* safety. The cytotoxicity of **1** against normal cells (HK-2) was evaluated experimentally (Fig. S5). The results showed cell viability of HK-2 cells treated with a DMSO solution of **1** with a concentration range from 8 mg L^{-1} to 128 mg L^{-1} was all more than 75%, exhibiting no significant cytotoxicity. Notably, the activity of cells treated with 256 mg L^{-1} of **1** displayed a significant decrease in cell viability to 50.56%, indicating clear cytotoxicity. In addition, the released *p*-phda ligand is nontoxic. For composites, HA and Fe(III)–TA films are also generally recognized as safe by the U.S. Food and Drug Administration.[70]

The biological samples used for the experiments were provided by Microbiology Institute of Shaanxi, Xi'an, Shaanxi, 710043, China.

Conclusions

Stimuli-responsive composites with the ability to respond to pH and HAase were constructed successfully and realized on-demand release of Ag^+ to target infection sites. The successful responsive antimicrobial activities depended on stimuli-triggered disassembly of coatings and excellent antimicrobial efficacy of the wrapped Ag(I) complex. The innovative design lies in the dual roles of the Ag(I) complex as the carrier and antimicrobial agent. The composites exhibit decreased Ag^+ leaching in non-infection environments and thereby minimize off-target effects, whereas they exhibit controlled and sustainable Ag^+ release upon exposure to an infection environment. The excellent antimicrobial efficacies originate from the high Ag^+ content of the Ag(I) complex, although Ag^+ release is suppressed partially by the extensive Ag–C bonds and Ag···Ag interactions. Therefore, the balance between high Ag^+ content and loose packing is crucial for the structural design of the Ag (I) complex.

The limitations of this work include the moderate pH-sensitive deconstruction of the Fe(III)–TA coating at pH 5.5. Thus, developing alternative approaches, such as adopting intrinsic pH-responsive Ag(I) complexes to promote acid sensitivity, can be considered in future works. Alternatively, external (exogenous) stimuli could provide more powerful control over the response, especially when the internal stimuli are not sufficiently effective. Dual- or multi-responsive platforms can be constructed to fully respond to various stimuli within the infection microenvironment (*i.e.* redox gradient, hormone levels, and glucose levels) and outside the physiological environment (*i.e.* temperature, light, and electric pulses). The synergy of response to multiple stimuli may further facilitate efficient and targeted Ag^+ release while reducing systemic toxicity and resource waste. These related strategies will be addressed in our further research.

Author contributions

Jing Han: conceptualization, writing – reviewing and editing, supervision, funding acquisition. Yue Hou: writing – original draft preparation, investigation. Zhong Yu: conceptualization, methodology, funding acquisition, investigation. Yi-xuan Chen: investigation. Jian-fei Xue: investigation. Yue-juan Zhang: methodology, investigation. Lei Gao: methodology, investigation. Yi Wan: methodology, funding acquisition, supervision.

Conflicts of interest

There are no conflicts to declare.

Data availability

The data supporting this article have been included as part of the supplementary information (SI). Supplementary information: details of additional IR, PXRD, crystallographic data, TG, diameters of inhibition zones, MICs and cell viability. See DOI: https://doi.org/10.1039/d5dt02724a.

CCDC 2409564 (**1**) contains the supplementary crystallographic data for this paper.[72]

Acknowledgements

This work is supported by the Science and Technology Plan Project of Shaanxi Province (No. 2019NY-201), the Foundation of Science and Technology in Shaanxi Province (No. 2020TD-050 and 2023-JC-YB-180) and the Science Foundation of Shaanxi Academy of Sciences (No. 2023K-01 and 2024P-15).

References

1 I. Atkinson, *Bioengineering*, 2022, **10**, 489.
2 X. Wang, S. Liu, M. Li, P. Yu, X. Chu, L. Li, G. Tan, Y. Wang, X. Chen, Y. Zhang and C. Ning, *J. Inorg. Biochem.*, 2016, **163**, 214.
3 R. Sugden, R. Kelly and S. Davies, *Nat. Microbiol.*, 2016, **10**, 16187.
4 R. Laxminarayan, A. Dusé, C. Wattal, A. Zaidi, N. Sumpradit, E. Vlieghe, G. L. Hara, I. Gould, H. Goossens and C. Greko, *Lancet Infect. Dis.*, 2013, **12**, 1057–1098.
5 Z. Hao, H. Lou, R. Zhu, J. Zhu, D. Zhang, B. S. Zhao, S. Zeng, X. Chen, J. Chan and C. He, *Nat. Chem. Biol.*, 2014, **10**, 21–28.

6 G. Wyszogrodzka, B. Marszałek, B. Gil and P. Dorożyński, *Drug Discovery Today*, 2016, **6**, 1009–1018.
7 S. Chernousova and M. Epple, *Angew. Chem., Int. Ed.*, 2013, **52**, 1636–1653.
8 C. Gunawan, W. Y. Teoh, C. P. Marquis and R. Amal, *ACS Nano*, 2011, **5**, 7214–7225.
9 E. Halevas, M. C. Nday, E. Kaprara, V. Psycharis and P. C. Raptopoulou, *J. Inorg. Biochem.*, 2015, **15**, 1150–1163.
10 C. B. Liu, Y. N. Gong, Y. Chen and H. L. Wen, *Inorg. Chim. Acta*, 2012, **383**, 277–286.
11 K. S. Kim, D. Lee, C. G. Song and P. M. Kang, *Nanomedicine*, 2015, **10**, 2709–2723.
12 J. R. Morones, J. L. Elechiguerra, A. Camacho, K. Holt, J. B. Kouri, J. T. Ramírez and M. J. Yacaman, *Nanotechnology*, 2005, **10**, 2346–2353.
13 K. B. Holt and A. J. Bard, *Biochemistry*, 2005, **44**, 13214–13223.
14 C. Marambio-Jones and E. M. V. Hoek, *J. Nanopart. Res.*, 2010, **5**, 1531–1551.
15 I. Saraeva, E. Tolordava, Y. Yushina, I. Sozaev, V. Sokolova, R. Khmelnitskiy, S. Sheligyna, T. Pallaeva, N. Pokryshkin, D. Khmelenin, A. Ionin, A. Semenova and S. Kudryashov, *Nanomaterials*, 2022, **21**, 3857.
16 S. S. Suner, M. Sahiner, E. Umut, R. S. Ayyala and N. Sahiner, *Pharmaceuticals*, 2023, **4**, 483.
17 C. N. Banti, A. D. Giannoulis, N. Kourkournelis and A. Owczarzak, *J. Inorg. Biochem.*, 2015, **142**, 132–144.
18 C. X. Zhao, J. N. Liu, B. Q. Li, D. Ren, X. Chen, J. Yu and Q. Zhang, *Adv. Funct. Mater.*, 2020, **36**, 2003619.
19 C. C. Piras, C. S. Mahon and D. K. Smith, *Chem. – Eur. J.*, 2020, **38**, 8452–8457.
20 X. Wang, K. Su, L. Tan, X. Liu, Z. Cui, D. Jing, X. Yang, Y. Liang, Z. Li, S. Zhu, K. W. K. Yeung, D. Zheng and S. Wu, *ACS Appl. Mater. Interfaces*, 2019, **11**, 15014–15027.
21 A. Hecel, P. Kolkowska, K. Krzywoszynska, A. Szebesczyk and H. Kozlowski, *Curr. Med. Chem.*, 2019, **4**, 624–647.
22 N. Duran, M. Duran, M. D. Jesus and G. Nakazato, *Nanomed. Nanotechnol.*, 2016, **3**, 789–799.
23 P. Horcajada, R. Gref, T. Baati, P. K. Allan, G. Maurin, P. Couvreur, R. E. Morris and C. Serre, *Chem. Rev.*, 2011, **2**, 1232–1268.
24 T. V. Slenters, I. Hauser-Gerspach, A. U. Daniels and K. M. Fromm, *J. Mater. Chem.*, 2008, **44**, 5359–5362.
25 M. Gawlik-Maj, A. Babczyńska, H. Gerber, J. Kotula, B. Sobieszczańska and M. Sarul, *Coatings*, 2022, **9**, 1338.
26 H. C. "Joe" Zhou and S. Kitagawa, *Chem. Soc. Rev.*, 2014, **16**, 5415–5418.
27 B. Đ. Glišić, L. Senerovic, P. Comba, H. Wadepohl, A. Veselinovic, D. R. Milivojevic, M. I. Djuran and J. Nikodinovic-Runic, *J. Inorg. Biochem.*, 2016, **155**, 115–128.
28 N. Durán, C. P. Silveira, M. Durán and D. S. Martinez, *J. Nanobiotechnol.*, 2015, **13**, 55.
29 Z. Yuan, S. Huang, S. Lan, H. Xiong, B. Tao, Y. Ding, Y. Liu, P. Liu and K. Cai, *J. Mater. Chem. B*, 2018, **48**, 8090–8104.
30 N. Yu, H. Peng, L. Qiu, R. Wang, C. Jiang, T. Cai, Y. Sun, Y. Li and H. Xiong, *Int. J. Biol. Macromol.*, 2019, **141**, 207–217.
31 Y. Zhang, P. Sun, L. Zhang, Z. Wang, F. Wang, K. Dong, Z. Liu, J. Ren and X. Qu, *Adv. Funct. Mater.*, 2019, **11**, 1808594.
32 C. Gorrini, I. S. Harris and T. W. Mak, *Nat. Rev. Drug Discovery*, 2013, **12**, 931–947.
33 J. Cao, T. Su, L. Zhang, R. Liu, G. Wang, B. He and Z. Gu, *Int. J. Pharm.*, 2014, **1–2**, 28–36.
34 S. Trombino, C. Servidio, F. Curcio and R. Cassano, *Pharmaceutics*, 2019, **8**, 407.
35 G. Y. Liu, M. Li, C. S. Zhu, Q. Jin, Z. C. Zhang and J. Ji, *Macromol. Biosci.*, 2014, **9**, 1280–1290.
36 Y. Zhang, Y. He, C. Shi, M. Sun and D. Shao, *ACS Sustainable Chem. Eng.*, 2020, **3**, 1695–1702.
37 S. Nastyshyn, J. Raczkowska, Y. Stetsyshyn, B. Orzechowska, A. Bernasik, Y. Shymborska, M. Brzychczy-Włoch, T. Gosiewski, O. Lishchynskyi, H. Ohar, D. Ochońska, K. Awsiuk and A. Budkowski, *RSC Adv.*, 2020, **17**, 10155–10166.
38 J. He, Y. Qiao, H. Zhang, J. Zhao and M. Zhou, *Biomaterials*, 2020, **234**, 119763.
39 J. Han, Q. Gao, Z. Yu, X. He, C. Y. Quan and M. Munakata, *Inorg. Chim. Acta*, 2014, **423**, 340–347.
40 J. Han, J. Yang, Z. Yu and Q. J. Wang, *Inorg. Chim. Acta*, 2018, **469**, 318–324.
41 J. Han, N. Ye, X. Zhang, Z. Yu and Y. Wan, *Inorg. Chim. Acta*, 2020, **512**, 119873.
42 J. Han, Y. X. Chen, Z. Yu, S. Li and Y. Wan, *Inorg. Chim. Acta*, 2024, **572**, 122290.
43 M. L. Chen, X. F. Xu, Z. X. Cao and Q.-M. Wang, *Inorg. Chem.*, 2008, **47**, 1877–1879.
44 Y. M. Lin, Z. J. Guan, K. G. Liu, Z. G. Jiang and Q. M. Wang, *Dalton Trans.*, 2015, **5**, 2439–2446.
45 Z. G. Jiang, K. Shi, Y. M. Lin and Q. M. Wang, *Chem. Commun.*, 2014, **18**, 2353.
46 N. J. Long and C. K. Williams, *Angew. Chem., Int. Ed.*, 2003, **23**, 2586–2617.
47 J. Manna, K. D. John and M. D. Hopkins, *Adv. Organomet. Chem.*, 1995, **38**, 79–154.
48 Z. Lei, X. K. Wan, S. F. Yuan, Z. J. Guan and Q. M. Wang, *Acc. Chem. Res.*, 2018, **10**, 2465–2474.
49 Z. Song, Y. Wu, Q. Cao, H. Wang, X. Wang and H. Han, *Adv. Funct. Mater.*, 2018, **23**, 1800011.
50 H. B. Yang, Z. Y. Yu, S. S. Ji, J. Yan, L. Han, Y. Liu, Y. J. Wang, Y. M. Niu, Q. Huo and M. Xu, *RSC Adv.*, 2022, **12**, 14707–14715.
51 Y. Yang, X. Wu, C. He, J. Huang, S. Yin, M. Zhou, L. Ma, W. Zhao, L. Qiu and C. Cheng, *ACS Appl. Mater. Interfaces*, 2020, **12**, 13698–13708.
52 G. M. Sheldrick, SHELX-97: Program Package for Crystal Structure Solution and Refinement, University of Göttingen, Göttingen, Germany, 1997.
53 O. V. Dolomanov, L. J. Bourhis, R. J. Gildea, J. A. K. Howard and H. Puschmann, *J. Appl. Crystallogr.*, 2010, **42**, 339–341.

54 L. Zhao, C. Q. Wan, J. Han, X. D. Chen and T. C. Mak, *Chem. – Eur. J.*, 2008, **14**, 10437–10444.
55 Y. Wang, C. T. He, Y. J. Liu, T. Q. Zhao, X. M. Lu, W. X. Zhang, J. P. Zhang and X. M. Chen, *Inorg. Chem.*, 2012, **51**, 4772–4778.
56 CLSI, *Method for antifungal disk diffusion susceptibility testing of yeasts, approved guideline*, USA, 2004, pp. 19087-1898.
57 M. Balouiri, M. Sadiki and S. K. Ibnsouda, *J. Pharm. Anal.*, 2016, **6**, 71–79.
58 A. Rocksin, G. F. Gerlach and S. Schwarz, *Berl. Munch. Tierarztl. Wochenschr.*, 2007, **120**, 42–49.
59 S. Magaldi, S. Mata-Essayag, C. Hartung de Capriles, C. Perez, M. T. Colella, C. Olaizola and Y. Ontiveros, *Int. J. Infect. Dis.*, 2004, **8**, 39–45.
60 J. Lorenzo-Morales, N. A. Khan and J. Walochnik, *Parasite*, 2015, **22**, 10.
61 J. Han, Y. D. Zhang, Z. Yu, X. He and B. Jin, *Z. Anorg. Allg. Chem.*, 2016, **642**, 584–589.
62 Z. Sun, F. Lv, L. Cao, L. Liu, Y. Zhang and Z. Lu, *Angew. Chem., Int. Ed.*, 2015, **54**, 7944–7948.
63 M. Grandoch, P. L. Bollyky and J. W. Fischer, *Circ. Res.*, 2018, **122**, 1341–1343.
64 Y. Xiao, D. Guo, T. Li, Q. Zhou, L. Shen, R. Li, Y. Xu and H. Lin, *Appl. Surf. Sci.*, 2020, **515**, 146063.
65 Y. Ju, J. Cui, M. Müllner, T. Suma, M. Hu and F. Caruso, *Biomacromolecules*, 2015, **16**, 807–814.
66 J. Han and S. C. Yong, *J. Korean Soc. Appl. Biol. Chem.*, 2010, **53**, 821–825.
67 H. P. Simmen and J. Blaser, *Am. J. Surg.*, 1993, **166**, 24–27.
68 Y. M. Zuo, X. Yan, J. Xue, L. Y. Guo, W. W. Fang, T. C. Sun, M. Li, Z. Zha, Q. Yu, Y. Wang, M. Zhang, Y. Lu, B. Cao and T. He, *ACS Appl. Mater. Interfaces*, 2020, **12**, 4333–4342.
69 M. Farré, K. Gajda-Schrantz, L. Kantiani and D. Barceló, *Anal. Bioanal. Chem.*, 2009, **393**, 81–95.
70 J. Jimenez, I. Chakraborty, M. Rojas-Andrade and P. K. Mascharak, *J. Inorg. Biochem.*, 2017, **168**, 13–17.
71 H. Ejima, J. J. Richardson, K. Liang, J. P. Best, M. P. V. Koeverden, G. K. Such, J. Cui and F. Caruso, *Science*, 2013, **314**, 154–157.
72 CCDC 2409564: Experimental Crystal Structure Determination, 2026, DOI: 10.5517/ccdc.csd.cc2lwbwq.